Journal of Alloys and Compounds 909 (2022) 164761

Contents lists available at ScienceDirect

Journal of Alloys and Compounds

journal homepage: www.elsevier.com/locate/jalcom

Microstructure and properties evolution of rolled powder metallurgy Cu-30Fe alloy

Chenzeng Zhang[a], Cunguang Chen[a,b,*], Pei Li[a], Mengjie Yan[a], Qian Qin[a], Fang Yang[a,**], Wenwen Wang[c], Zhimeng Guo[a,b], Alex A. Volinsky[d,e,***]

[a] *Institute for Advanced Materials and Technology, University of Science and Technology Beijing, Beijing 100083, PR China*
[b] *State Key Laboratory for Advanced Metals and Materials, University of Science and Technology Beijing, Beijing 100083, PR China*
[c] *Technical Support Center for Prevention and Control of Disastrous Accidents in Metal Smelting, University of Science and Technology Beijing, Beijing 100083, PR China*
[d] *National Research Tomsk State University, 36 Lenin Ave., Tomsk 634050, Russia*
[e] *Department of Mechanical Engineering, University of South Florida, 4202 E. Fowler Ave., ENG 030, Tampa, FL 33620, USA*

ARTICLE INFO

Article history:
Received 29 January 2022
Received in revised form 11 March 2022
Accepted 23 March 2022
Available online 1 April 2022

Keywords:
Metals and alloys
Powder metallurgy
Mechanical alloying
Microstructure
Mechanical properties

ABSTRACT

Powder metallurgy Cu-30Fe alloy was prepared by mechanical alloying, pressureless sintering, and rolling processes. The alloy microstructure and physical properties affected by rolling were studied. The Fe particles were small and uniformly distributed in the Cu matrix. The average Fe particle size in the sintered state was 1 µm, and particles had subspherical or irregular shapes. The Fe particles became elongated, tadpole-shaped, and spindle-shaped as a result of rolling. At the same time, the Cu grains were elongated and refined, while the Cu grains near the Fe particles were finer as a result of the coordinated deformation of the soft Cu and hard Fe phases. After annealing at 400 °C, the cold-rolled Cu-30Fe alloy had 620 MPa tensile strength, 10% elongation, and 50% IACS electrical conductivity, achieving a good combination of mechanical and functional properties. The coordinated deformation behavior and grain refinement mechanisms of both Cu and Fe phases due to rolling were described, along with the microstructure and physical properties evolution.

1. Introduction

As novel structural and functional metallic materials, Cu-Fe alloys have been widely used in many fields, including 5G communications, electromagnetic shield construction materials, conductive spring materials, aerospace special solders, and information tags, due to high strength, favorable electrical and thermal conductivity, and excellent electromagnetic shielding properties [1–4]. Cu-Fe alloys are considered to be metastable immiscible alloys due to the Cu and Fe components with distinct properties and high positive enthalpy values [5]. Based on the Cu-Fe phase diagram, Cu and Fe phases are insoluble at room temperature, but there is a liquid phase immiscibility area at elevated temperature. When the large-size Cu-Fe alloys with higher than 10 wt% Fe contents are prepared by traditional casting, the melt will undergo a two-phase separation, unavoidably passing through the liquid phase separation zone during solidification. As a result, Cu-rich and Fe-rich zones are created, and the severe composition segregation and dendrite-like Fe particles can predictably deteriorate the alloy's performance [6]. Therefore, the segregation and coarsening of Fe particles have become key factors restricting the development and applications of Cu-Fe alloys.

Over the years, many researchers have tried to obtain promising Cu-Fe alloys with uniform microstructure and high performance. Jeong et al. [7,8] studied the effects of Si on the microstructure and mechanical properties of the Cu-10Fe alloy and found that when the amount of Si was 2 wt%, the yield strength increased by 95 MPa because of the microstructure refinement and the spherical Fe particles with 10 µm size. Kim and Yuan et al. [9,10] discovered that the addition of Mg significantly refined the Fe phase, inhibited its dendrite segregation, and improved the mechanical properties of the alloy. Liu et al. [11] demonstrated that the addition of B in the

---

[*] Corresponding author at: Institute for Advanced Materials and Technology, University of Science and Technology Beijing, Beijing 100083, PR China.
[**] Corresponding author.
[***] Corresponding author at: National Research Tomsk State University, 36 Lenin Ave., Tomsk 634050, Russia.
E-mail addresses: cgchen@ustb.edu.cn (C. Chen), yangfang@ustb.edu.cn (F. Yang), volinsky@usf.edu (A.A. Volinsky).

https://doi.org/10.1016/j.jallcom.2022.164761
0925-8388/Published by Elsevier B.V.

Cu-20Fe alloy promoted liquid-liquid phase separation, that both the volume fraction and average size of Fe-rich spherulite increased, and that the magnetic properties of the alloy were significantly improved. Pang et al. [12] found that the addition of Si promoted the precipitation and refinement of the Fe phase, improving the mechanical and physical properties of the Cu-Fe alloy. Zhang et al. [13] reported that the addition of Nb to the Cu-Fe alloy increased its strength and fracture elongation. Several researchers of the Cu-Fe systems used double melt mixed casting [14,15], laser cladding [16–18], selective laser melting [19–21], and severe plastic deformation [22,23]. It thus appears that the addition of micro-alloying elements and the improvement of the process can reduce the two-phase segregation, refine the microstructure, and enhance the mechanical and physical properties. However, the Fe particles in Cu-Fe alloys prepared by these methods are still relatively coarse or unevenly distributed, and they are not suitable for manufacturing large-size samples with uniform microstructure and fine Fe particles for industrial applications.

Comparatively, powder metallurgy (PM) has the natural advantages of homogeneous microstructure and fine grains. Therefore, it is of great practical interest to make the PM Cu-Fe alloys. Abbas et al. [24,25] utilized gas atomized Cu-Fe alloy powder with different Fe contents to prepare Cu-Fe alloys with an average size of 2–5 μm consolidated by spark plasma sintering (SPS), and confirmed that refining Fe particles can improve electrical and magnetic properties. Wang et al. [26] prepared Cu-15Fe alloy with fine and evenly distributed Fe particles by powder metallurgy, which showed that the refinement of Fe particles could improve the mechanical and electrical conductivity of the alloy. Current research of PM Cu-Fe alloys has mainly focused on the gas atomization powder and SPS processing, with the problems of high cost and dimensional restrictions. Furthermore, Cu and Fe are soft and hard phases with different deformation behavior, and thus large shear strains would occur at the interface between the Fe phase and Cu matrix during cold rolling. Predictably, the shape and size of the original Fe particles will affect the coordinated deformation of the two phases, thereby affecting the properties of the alloy. However, researchers have not paid much attention to the deformation behavior of the PM Cu-Fe alloys. In this paper, PM Cu-30Fe alloy was prepared by mechanical alloying, cold isostatic pressing, vacuum sintering, and rolling. The evolution of deformation behavior and properties due to rolling were investigated. This study can guide the industrial applications of PM Cu-Fe alloys with high Fe content.

2. Experimental procedure

2.1. Samples preparation

The raw materials utilized were electrolytic Cu powder (D_{50} = 10 μm, GRIPM Advanced Materials Co., Ltd., China), and carbonyl Fe powder (D_{50} = 10 μm, GRIPM Advanced Materials Co., Ltd., China). Mechanical alloying for fabricating Cu-30Fe (wt%) powder was performed in a stainless-steel mixing jar containing stainless-steel balls with a ball-to-powder weight ratio of 10:1 and milling time of 16 h at room temperature. The jar was filled with argon (99.99% pure) and then a GN-2 high-energy vibration ball mill was used. Stearic acid with 1 wt% content as a process control agent was added to prevent powders from sticking to the mixing jar walls during ball milling. To avoid oxidation of raw powders before transfer to stainless-steel jars, the raw materials were stored in a glove box filled with high purity argon gas and the loading of the powder was completed in this box. The ball-milled powders were annealed in a hydrogen atmosphere at 500 °C for 1 h to improve the formability of the powders. Subsequently, cold isostatic pressing at 200 MPa was conducted to obtain green bodies with 100 mm × 100 mm × 12 mm dimensions. The sintering process was performed at 1000 °C for 2 h in a vacuum sintering furnace (10^{-2} Pa, HTS-1500) with a 5 °C/min heating rate. Pure titanium powder as oxygen absorber was placed around the green samples but not in contact with them during sintering. Hot rolling was performed at 800 °C to reduce the thickness of the samples from 12 mm to 3 mm by multi-pass rolling and achieved a 75% reduction rate. Subsequently, cold rolling was conducted at room temperature to reduce the thickness of the samples from 3 mm to 0.5 mm by multi-pass rolling with an 83% reduction rate. Finally, the cold-rolled samples were annealed at 400 °C and 600 °C for 1 h, respectively.

2.2. Characterization

X-ray diffraction (XRD, Rigaku TTR III) was used to investigate the phases' composition. The microstructure and composition of PM Cu-30Fe alloys were analyzed by field emission scanning electron microscopy (FESEM, Zeiss Supra 55) with energy dispersive spectroscopy (EDS). Electron backscatter diffraction (EBSD) was used to characterize the microstructure from the rolling direction plane of the cold-rolled sheets. The size of the samples used for cross-sectional polishing and EBSD was 10 mm × 10 mm with 5 mm thickness. The observations by scanning transmission electron microscopy (STEM, FEI Talos F200X) were performed by a microscope operated in the high-angle annular dark-field (HAADF) mode at 200 kV. To identify the composition and structure of precipitated nanoparticles, they were examined by high-resolution transmission electron microscopy (HRTEM). Room temperature tensile tests of samples were conducted using the AGI-250KN tensile testing machine according to the ASTM-E08 standard. The electrical conductivity of the specimens was measured by the four-point probe method (TH2513A) at room temperature.

3. Thermodynamic analysis of the Cu-Fe system

The thermodynamic analysis is the theoretical basis for the study of alloy systems, so the thermodynamic calculations of the Cu-Fe binary alloy system were carried out first. For a binary alloy system, the change of Gibbs free energy of solid solution formed by pure components A and B can be expressed as:

$$\triangle G = \triangle H - T\triangle S \tag{1}$$

where ΔG is the Gibbs free energy, ΔH is the mixing enthalpy for a mixture of pure A and B elements to form a disordered A(B) solid solution, ΔS is the mixing entropy forming disordered solid solution, and T is the temperature of the formation of solid solution. △S can be expressed as:

$$\triangle S = -R\,(x_A \ln x_A + x_B \ln x_B) \tag{2}$$

where R is the ideal gas constant, and x_A and x_B are the mole fractions of elements A and B, respectively. According to the Miedema's semi-empirical model, the enthalpy of the formation of the solid solution consists of the three parts [27,28]:

$$\triangle H_{total} = \triangle H_{chemical} + \triangle H_{elastic} + \triangle H_{structural} \tag{3}$$

where $\triangle H_{total}$ is total enthalpy, $\triangle H_{chemical}$ is the chemical contribution, $\triangle H_{elastic}$ is the elastic mismatch energy due to size mismatch, and $\triangle H_{structural}$ is the lattice stability energy due to structural changes of the solid solution formation. For the A-B binary alloy system, $\triangle H_{chemical}$ can be expressed as:

$$\triangle H_{chemical} = \frac{2Pf\left(C^S\right)\left(x_A V_A^{2/3} + x_B V_B^{2/3}\right)}{\left(n_{ws}^{A}\right)^{-1/3} + \left(n_{ws}^{B}\right)^{-1/3}}\left[-(\triangle\Phi^*)^2 + \frac{Q}{P}\left(\triangle n_{ws}^{1/3}\right)^2 - \frac{S}{P}\right] \tag{4}$$

Here, V is the molar volume, Φ* is the work function, n_{ws} is the electron density of constituent elements, Q, P and S are the empirical constants related to constituent elements, and $f(C^S)$ is the concentration function, which can be calculated for solid solutions as:

$$f(C^S) = \frac{x_A V_A^{2/3}}{x_A V_A^{2/3} + x_B V_B^{2/3}} \frac{x_B V_B^{2/3}}{x_A V_A^{2/3} + x_B V_B^{2/3}} \tag{5}$$

$\triangle H_{elastic}$ can be expressed as in [29]:

$$\triangle H_{elastic} = x_A\, x_B\, (x_A \triangle E_{A\ in\ B} + x_B \triangle E_{B\ in\ A}) \tag{6}$$

$$\triangle E_A \text{in B} = \frac{2K_A\, G_B (\triangle V)^2}{3K_A\, V_B + 4G_B\, V_A} \tag{7}$$

$$\triangle E_B \text{in A} = \frac{2K_B\, G_A (\triangle V)^2}{3K_B\, V_A + 4G_A\, V_B} \tag{8}$$

Here, $\triangle E_A$ in B and $\triangle E_B$ in A are the changes in elastic energy due to A dissolved in B and B dissolved in A, K is the bulk modulus and G is the shear modulus.

$\triangle H_{structural}$ is a very small value related to the number of valance electrons per atom, which can be neglected in the estimation of ΔH_m. In this study, mechanical alloying is a non-equilibrium process, which may lead to the formation of amorphous rather than a solid solution. For amorphous solution, since there is no long-range ordered crystal structure, $\triangle H_{elastic}$ and $\triangle H_{structural}$ are negligible, and their enthalpy changes can be expressed as in [28,29]:

$$\triangle H_{amorphous} = \triangle H_{chemical} + \alpha (x_A T_m^A + x_B T_m^B) \tag{9}$$

Here, α is 3.5 J mol^{-1} K^{-1}, and T_m are the melting temperatures of A and B elements. The values of the corresponding parameters are listed in Table 1. According to the Miedema model, the enthalpy change and the Gibbs free energy of solid solution and amorphous solution formed by different Fe contents in the Cu-Fe binary alloy system can be calculated at any temperature.

Fig. 1 shows the enthalpy ΔH, entropy ΔS, and Gibbs free energy ΔG for the formation of solid solution and amorphous phases in the Cu-Fe system as functions of Fe mole fraction, calculated by using the Miedema model at room temperature (T = 293 K). It can be seen in Fig. 1 that the value of $\triangle H_{elastic}$ is almost zero and is nearly unchanged, which is due to almost the same atomic radii of Cu (1.28 Å) and Fe (1.26 Å), the similar electronegativity of the two atoms, and the small elastic distortion energy caused by the formation of substitutional solid solution. Therefore, the $\triangle H_{total}$ of Cu and Fe is mainly dominated by $\triangle H_{chemical}$. $\triangle G_{ss}$ and $\triangle G_{amorphous}$ are positive and $\triangle G_{amorphous} > \triangle G_{ss}$, indicating that Cu and Fe do not dissolve in each other in equilibrium, and sufficient external energy is needed for the formation of a solid solution. Because the free energy of the amorphous form of Cu and Fe is higher than the solid solution, the solid solution is thermodynamically stable and easier to form than the amorphous phase. When the Fe content is 0.3, $\triangle H_{total}$ reaches 14.84 kJ/mol, and $\triangle G$ is 13.35 kJ/mol. Mechanical alloying can provide a certain amount of energy to expand the solid solubility of the Cu-Fe binary immiscible system and form a supersaturated solid solution [30–34]. The XRD and EDS spectra in the following results section confirm this.

Table 1
Required parameters for thermodynamic analysis according to the Miedema model of the Cu-Fe system [15–17].

Parameter	Cu	Fe
Φ* (V)	4.45	4.93
V (cm^3 mol^{-1})	7.12	7.09
n_{ws} (cm^{-1})	3.18	5.55
K (10^{10} N m^{-2})	13.7	16.8
G (10^{10} N m^{-2})	4.8	8.15
T_m (K)	1356.6	1808

P = 14.1 kJV^{-2} cm^{-1}, S/P = 0 and Q/P = 9.4.

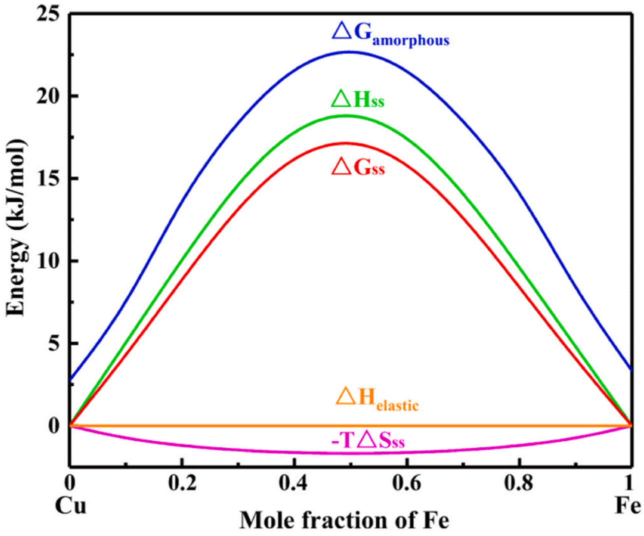

Fig. 1. Enthalpy ΔH, entropy ΔS, and Gibbs free energy ΔG for the formation of solid solution and amorphous phases in the Cu-Fe system calculated by using the Miedema model.

4. Results

4.1. Powder characterization

Fig. 2 shows the morphology of electrolytic Cu powder, carbonyl Fe powder, and mechanically alloyed Cu-Fe powder. Electrolytic Cu powder has an irregular shape and an average particle size of about 10 μm in Fig. 2a, while carbonyl Fe powder smaller than 10 μm has a spherical shape in Fig. 2b. Fig. 2c shows the mechanically alloyed Cu-Fe powder with a flake shape and a size smaller than 10 μm.

Fig. 3 shows the XRD spectra of the mechanically alloyed Cu-Fe powder. It can be seen that the supersaturated solid solution of Fe is formed in Cu after ball milling. A small hump can be found in Fe diffraction reflection after ball milling since part of Fe still existed in the form of a single phase without a solid solution. According to the previous thermodynamic calculations, the $\triangle H_{chemical}$ generated between Cu and Fe after the formation of the solid solution had a large positive value, shifting the Cu diffraction reflection to a smaller angle. After annealing, the solid-solution Fe in the Cu-Fe powder precipitated from the Cu lattice, which led to the enhancement of the Fe diffraction reflection. The cross-section EDS spectra of the Cu-30Fe powder after ball milling in Fig. 4 show that the element distribution of Cu and Fe can completely coincide. This indicated that Fe was uniformly dissolved in Cu after ball milling, which was consistent with the XRD results in Fig. 3.

4.2. Microstructure evolution

4.2.1. SEM analysis

Fig. 5 shows the SEM images of Cu-30Fe sintered samples in backscatter diffraction mode. The bright area is the Cu matrix, the gry area is Fe particles, and the black part is pores. The relative density of the sintered sample is 80.6% of the Cu-30Fe alloy theoretical density. The Fe particles were uniformly distributed in the Cu matrix without obvious composition segregation. Most of the Fe particles were submicron in size, while some larger particles were 4 μm. Most of the Fe particles were subspherical in shape, and a small amount of irregularly shaped Fe particles were present. Compared with Cu-Fe alloys prepared by conventional casting, the

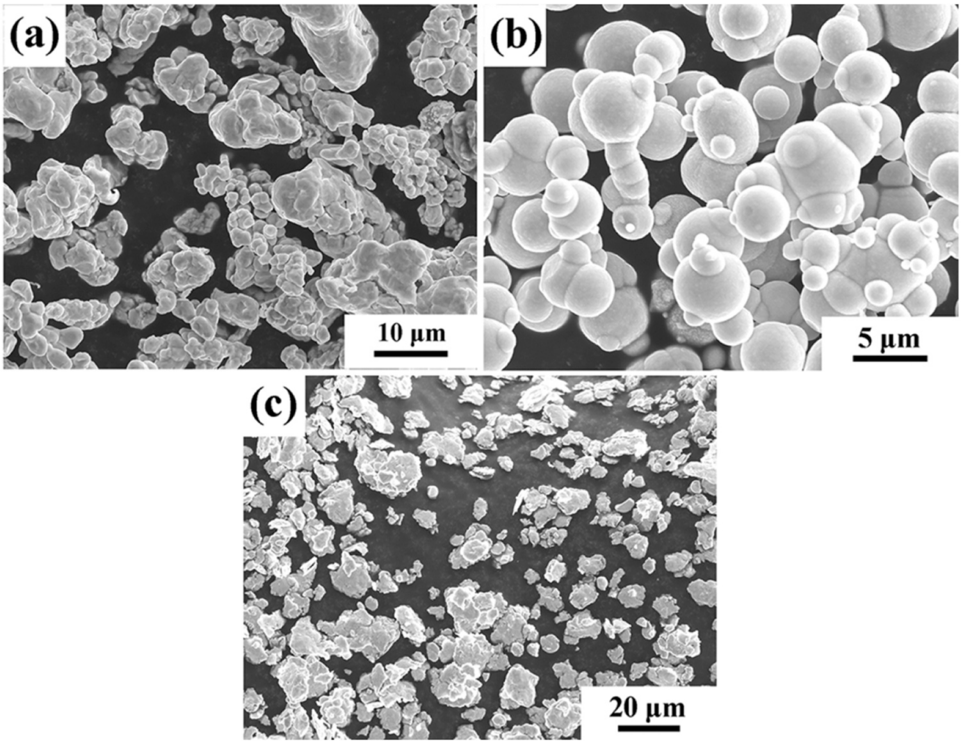

Fig. 2. SEM images of raw powders: (a) Electrolytic Cu powder; (b) Carbonyl Fe powder and (c) Mechanically alloyed composite powder.

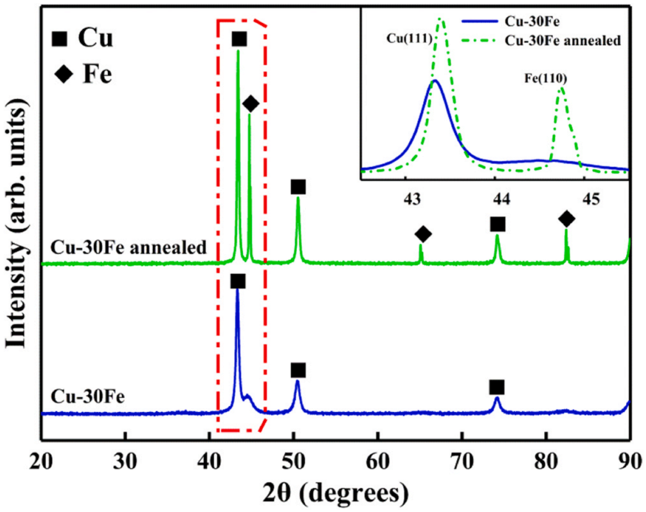

Fig. 3. XRD patterns of composite powder after ball milling and annealing.

original microstructure of Cu-Fe alloys in this study had considerable advantages [7–13]. In general, fine, spherical, and uniformly distributed Fe particles were the key to the preparation of high-performance Cu-Fe alloys.

Fig. 6 shows the SEM images of the transverse and longitudinal sections of Cu-30Fe alloys in the hot-rolled and cold-rolled states. After hot rolling, the relative density of the sample reached 98.3% of the theoretical density. After cold rolling, the relative density reached 99.6% of the theoretical density, achieving almost full density. Fe particles in the hot-rolled normal direction (ND) were not significantly deformed, still having a nearly spherical or irregular shape, while Fe particles in the transverse direction (TD) were elongated along the rolling direction, distributed in strips. The deformation of Fe particles with different sizes was uneven, and the deformation of smaller Fe particles was more severe than the larger ones. At the same time, the number of black pores was significantly reduced, which indicated an increase in density. Overall, the morphology of Fe particles in hot rolling was related to the work hardening, dynamic recovery, and recrystallization during deformation. The distribution of Fe particles in the cold-rolled ND surface showed

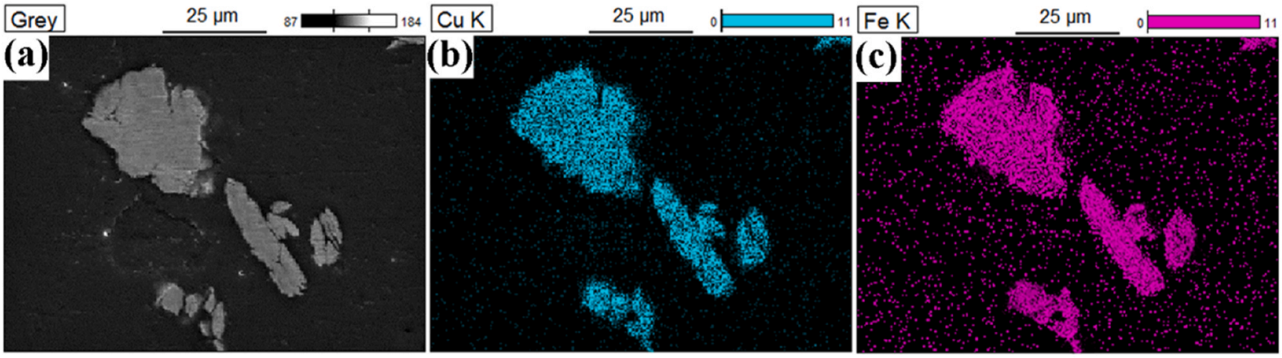

Fig. 4. EDS spectra maps of the cross-section of the Cu-30Fe composite powders after mechanical alloying: (a) SEM image; (b) Cu map; (c) Fe map.

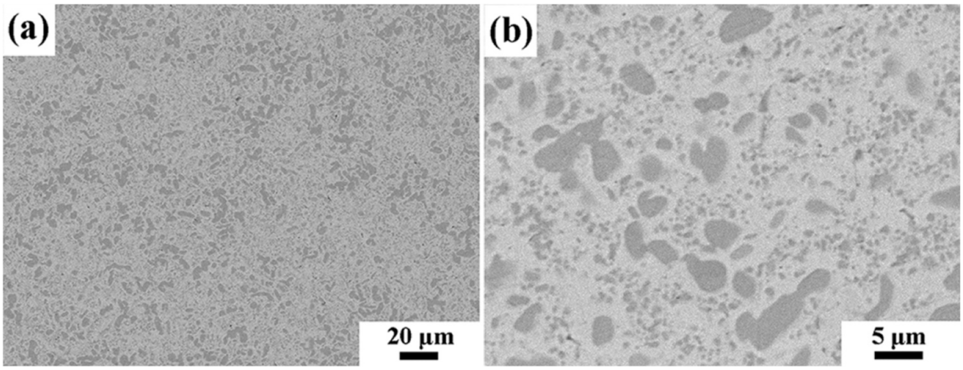

Fig. 5. SEM images of sintered Cu-30Fe alloy: (a) low magnification, and (b) high magnification.

directionality, and the degree of deformation was low. The degree of deformation of Fe particles in the TD surface was large, and most of the particles were elongated along the rolling direction, but the particle morphology was different, mainly spherical, elongated, tadpole-shaped, and spindle-shaped. The morphological difference of Fe particles in the hot rolling and cold rolling processes was related to the composition of Fe particles, their size, and the cooperative deformation mechanism of Cu-Fe soft and hard phases, which is discussed in detail further.

4.2.2. EBSD analysis

Fig. 7 shows the EBSD maps of the longitudinal section of the Cu-30Fe alloy in the cold-rolled state. Fig. 7a and Fig. 7b show the phase distribution and the grain boundary distribution, respectively. The blue area in Fig. 7a is the Cu phase and the red area is the Fe phase. The thick and black lines in Fig. 7b are the high angle grain boundaries (HAGBs, > 15°) and the thin and red lines are the low angle grain boundaries (LAGBs, < 15°). Fig. 7c and Fig. 7d show the inverse pole figure (IPF) maps corresponding to the grain orientation distribution of the Cu phase and Fe phase, respectively. The EBSD results show that after large cold rolling deformation, both Cu and Fe grains were elongated and broken to form ultra-fine grains. The average grain sizes of Cu and Fe phases were 0.54 μm and 0.57 μm, respectively. Abundant HAGBs and LAGBs were generated in the grain boundary of the Cu matrix and the Cu/Fe phase boundary. The LAGBs were produced in the Fe phase. The color change could be observed in some Fe grains, which could indicate that the Fe grains were rotated by the stress. The Cu and Fe grains produced deformation flow lines along the rolling direction, and the grains were banded. The Cu grains were broken and fractured to form smaller sub-crystals due to severe deformation. The Fe grains were deformed along the rolling direction due to the presence of higher stress to produce more and smaller sub-crystalline grains. A large number of dislocation entanglements, fine sub-crystals, and fibrous structures were generated along the rolling direction. The deformation degree of the Cu matrix was significantly larger than Fe

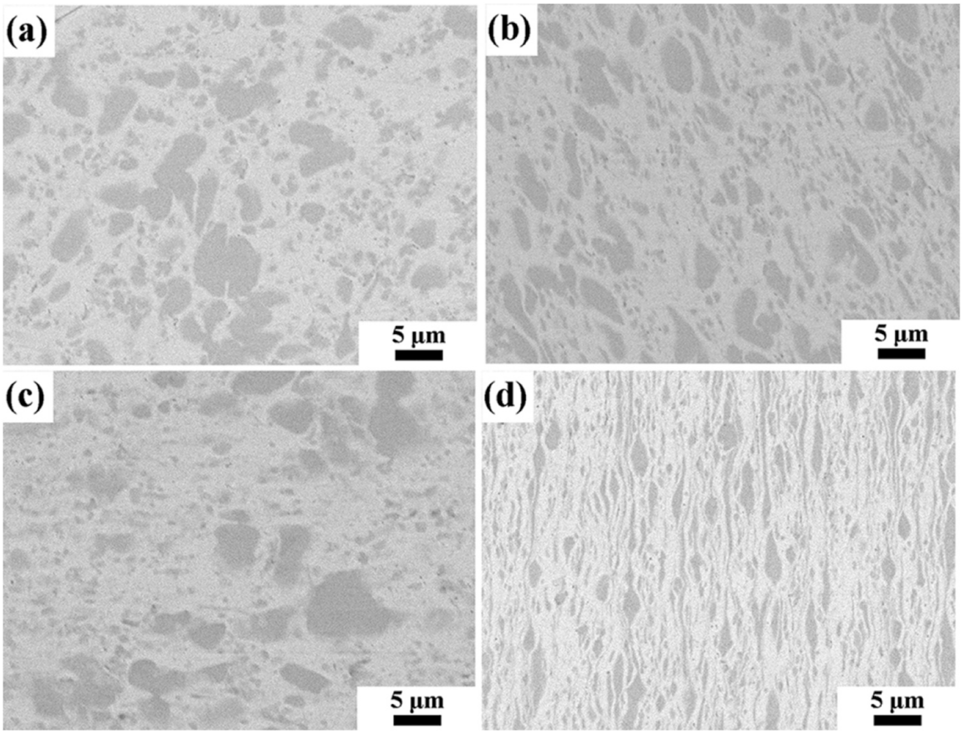

Fig. 6. SEM images of the Cu-30Fe alloy in hot rolled and cold rolled states: (a) Transverse section of the hot-rolled sample; (b) Longitudinal section of the hot-rolled sample; (c) Transverse section of the cold-rolled sample; (d) Longitudinal section of the cold-rolled sample.

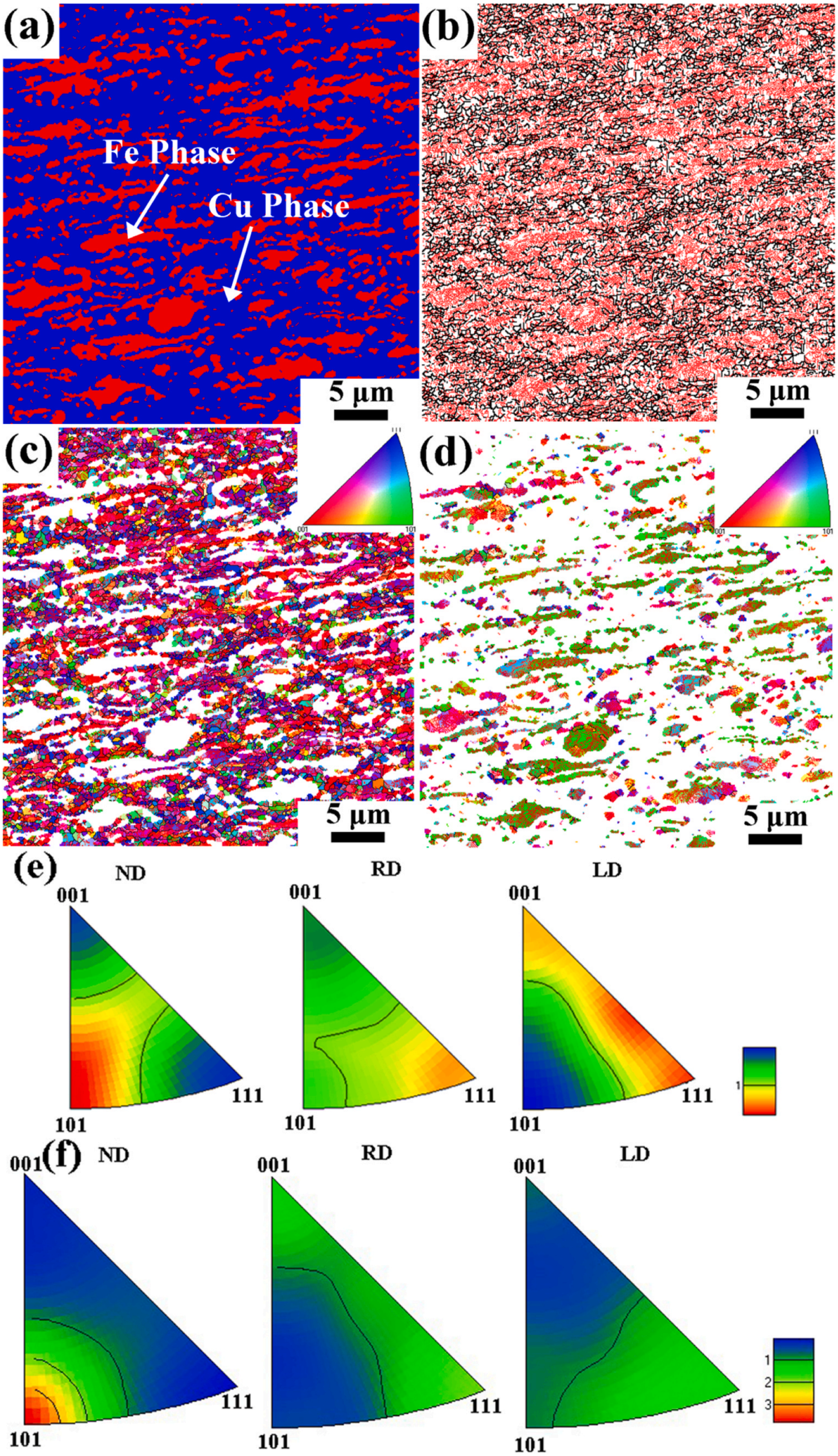

Fig. 7. EBSD images in longitudinal section of the cold-rolled Cu-30Fe alloy: (a) Phase distribution diagram; (b) Large and small-angle grain boundary map; (c) Inverse pole figures of the Cu; (d) Inverse pole figures of the Fe; (e-f) IPF diagrams of Cu and Fe, respectively.

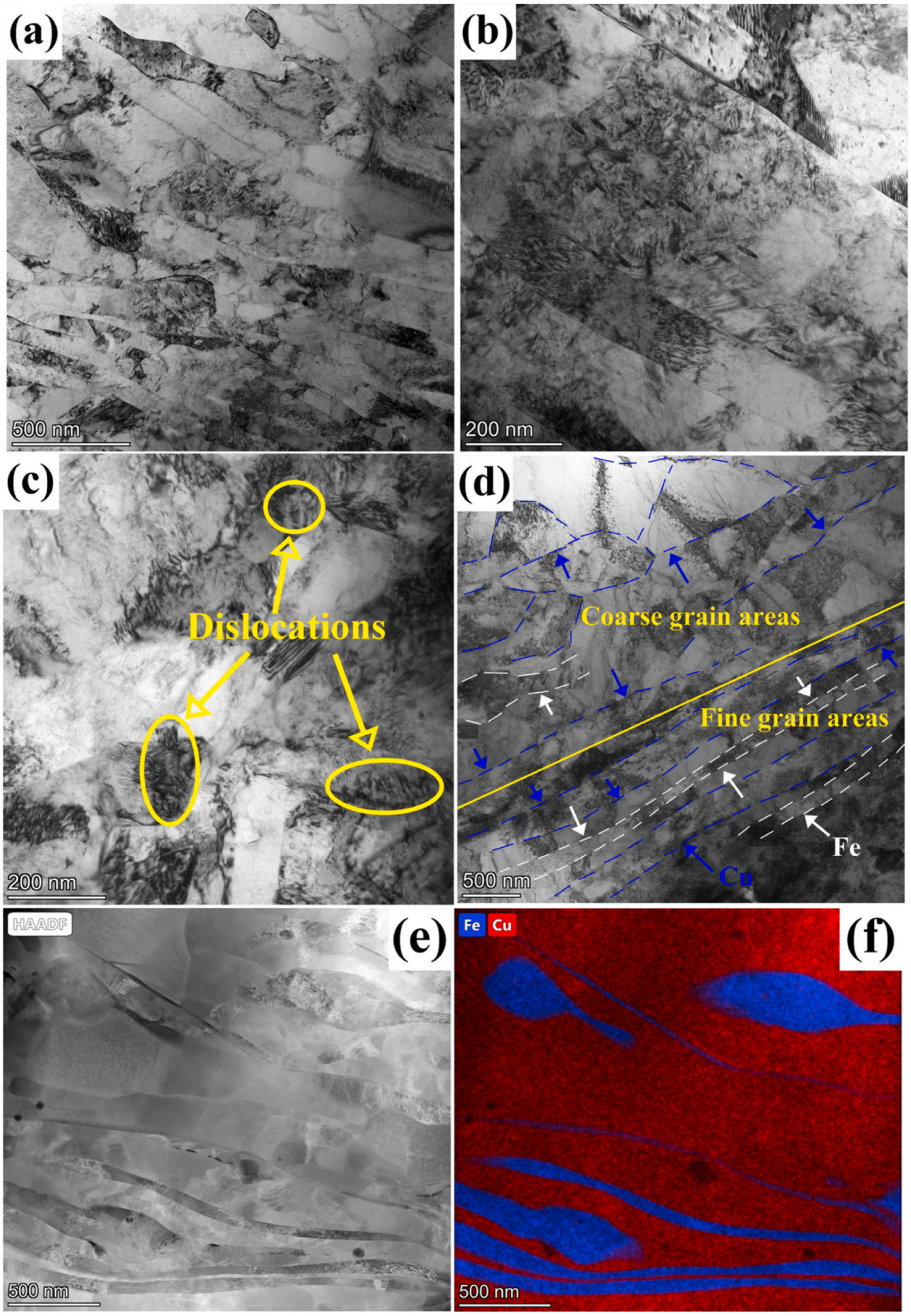

Fig. 8. TEM images in longitudinal section of the cold-rolled Cu-30Fe alloy: (a-d) Bright-field images; (e) HAADF image; (f) Fe and Cu map. The Cu and Fe grains in (d) are distinguished by blue and white dashed lines, respectively.

particles. Fig. 7d and Fig. 7e are IPF maps of Cu and Fe, respectively. It can be seen that the two phases have distinct texture, the {110} < 111 > texture in the Cu matrix, and the {110} < 001 > and {110} < 111 > textures in Fe particles.

4.2.3. TEM analysis

Fig. 8 shows the TEM images of the longitudinal section of the Cu-30Fe alloy in the cold-rolled state. It can be seen that the fibrous Fe grains and Cu grains were elongated along the rolling direction, dozens of nanometers thick. A large number of dislocations can be observed distributed within the Cu and Fe grains. Many precipitated Fe nanoparticles can be observed in Fig. 8b in the form of short rods, distributed in the dislocation forest inside Cu grains and around the grain boundaries. These Fe nanoparticles were precipitated at the defects such as grain boundaries and dislocations during sintering and rolling and interacted with the dislocations generated by the deformation to strengthen the matrix. In addition, it can be found that there are more obvious areas containing fine and coarse grains in the elongated lamella structure in Fig. 8d, the Cu and Fe grains were depicted by blue and white dashed lines, respectively. This was due to the mechanism of grain refinement influenced by the co-ordinated deformation of soft Cu and hard Fe phases. Fig. 8e and Fig. 8f show that the precipitated Cu-rich phase could be found inside the Fe particles, especially in the local area, where it was

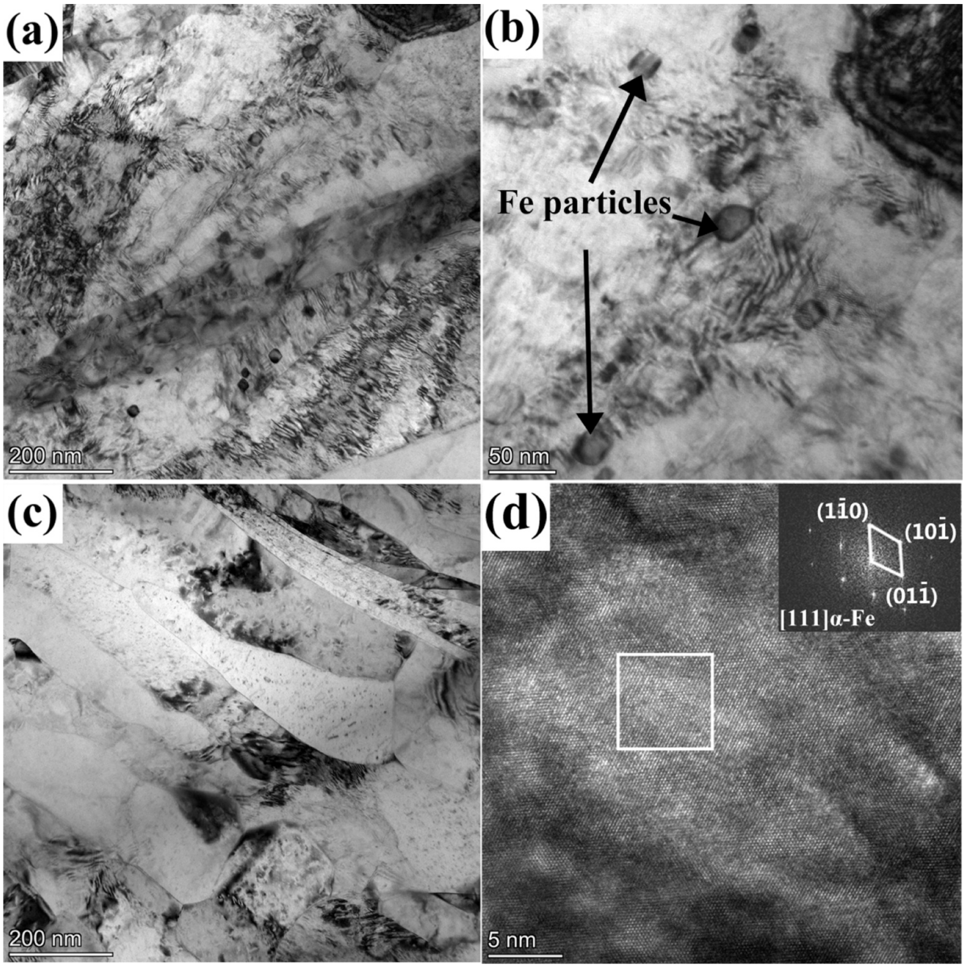

Fig. 9. TEM images of the Cu-30Fe alloy after annealing at 400 °C in the longitudinal section: (a-c) Bright-field images; (d) HRTEM and diffraction spots images.

difficult to deform (such as the tadpole-shaped head). It can be also found that these Cu-rich precipitated phases were mainly distributed in the dislocation network of Fe particles. These precipitated phases had a strong nailing effect on the internal dislocation slip of Fe particles, which led to the local area of the Fe particles containing Cu precipitated phases with increased strength and deformation resistance. As a result, peculiar shapes such as tadpole shapes were formed. The dislocation density was higher in the Cu matrix near the Fe particles with finer grains, and lower in the Cu matrix far from the Fe particles.

Fig. 9 shows the TEM images of the longitudinal section of the Cu-30Fe alloy in the cold-rolled state after annealing at 400 °C. Fig. 9a shows that a lot of nano-sized Fe particles are distributed in the Cu matrix, and the number of particles has increased compared to that before annealing. It can be indicated that some Fe particles have been precipitated in the Cu matrix after annealing. The presence of strain-induced streaks in the Cu matrix around these Fe particles in Fig. 9b indicates that the Fe particles have a high resistance to the motion of dislocations and exhibit a strong pegging effect on dislocations. After annealing, the recovery occurred in the matrix, the dislocation density decreased significantly, and more fine precipitation phases were produced in the grains, as seen in Fig. 9c. Fig. 9d is the HRTEM image of the fine precipitated phase in the matrix. The crystal structure analysis of the diffraction spot confirmed that the precipitated phase was α-Fe.

Fig. 10 shows the HRTEM image of the interface between the precipitated Fe nanoparticle and the Cu matrix. The plane spacing of the precipitated nanoparticles is 0.201 nm, corresponding to the

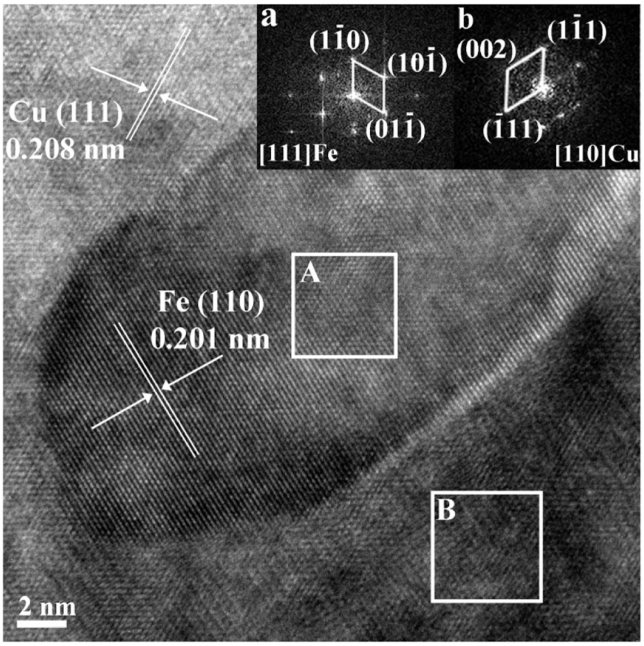

Fig. 10. HRTEM image of the precipitated Fe nanoparticle and the Cu matrix.

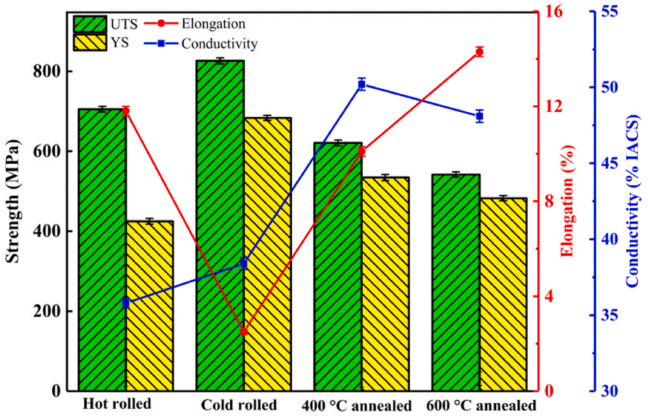

Fig. 11. Mechanical properties and electrical conductivity of Cu-30Fe alloys in different states.

(110) plane spacing of Fe, and the plane spacing of the Cu matrix is 0.208 nm, corresponding to the (111) plane spacing of Cu. Therefore, it can be seen from the plane spacing and diffraction patterns that the precipitated nanoparticles are body-centered cubic α-Fe, and the matrix is the face-centered cubic Cu phase. The orientation relationship between the precipitated nanoparticles and the matrix is $(111)_{Cu}//(110)_{Fe}$, $[110]_{Cu}//[111]_{Fe}$, which conforms to the typical K-S orientation relationship. The mismatch degree of the matrix and precipitated phase can be calculated as [23]:

$$\delta = \frac{2(d_1 - d_2)}{(d_1 + d_2)} \tag{10}$$

Here, δ is the mismatch between the matrix and the nanoparticles, d_1 is the plane spacing of $(111)_{Cu}$ and d_2 is the plane spacing of $(110)_{Fe}$. The misfit parameter for the semi-coherent region varies from 0.05 to 0.25, the misfit parameter for the non-coherent region is larger than 0.25, and the misfit parameter for the coherent region varies from 0 to 0.25 [35]. Here, the value of δ is 0.034, falling into the semi-coherent region (0.025–0.25), so the $(110)_{Fe}$ and $(111)_{Cu}$ have a semi-coherent relationship.

4.3. *Mechanical and electrical properties of the Cu-30Fe alloy*

Fig. 11 shows the variation of mechanical properties and electrical conductivity of Cu-30Fe alloys in different states. After cold rolling, the tensile strength of the Cu-30Fe alloy was 826 MPa, the elongation was 2.5%, and the electrical conductivity was 38.4% IACS. After low-temperature annealing, the tensile strength decreased, while the elongation and electrical conductivity increased. After 400 °C annealing for 1 h, the tensile strength was 621 MPa, the elongation was 10.1%, and the electrical conductivity was 50.2% IACS, demonstrating the optimal comprehensive performance. After cold rolling, the alloy had a large number of dislocations with high internal stress due to process hardening. After annealing, the recovery of the matrix took place, and the dislocation density decreased. Accordingly, the alloy softened, and nanoscale Fe particles precipitated from the Cu matrix. Therefore, the electrical conductivity of the alloy increased.

5. Discussion

5.1. *Two-phase deformation mechanism*

Due to the different mechanical properties of metals, the soft and hard phases exhibit different and interactive deformation behavior when deformed simultaneously, with fractures occurring in the hard phase [36,37]. Plastic instability is affected by the shape, strength, and strain hardening exponents of the layers [37,38]. To compare the flow properties of the constituents, the strength coefficient, k, strain-hardening exponent, n, and tensile strength for Cu and Fe are summarized in Table 2. These values are obtained from the tensile tests after annealing each specimen. It can be seen that Fe has higher strength (252 MPa) and lower strain-hardening exponent (0.215) compared with Cu. In the Cu-Fe two-phase system in this study, the Cu matrix surrounded the Fe phase, and the Fe phase would be deformed synergistically with the Cu matrix as a hard phase. From the SEM image in Fig. 5, it could be seen that in the initial sintered state, the Fe phase particles were uniformly distributed in the Cu matrix with an average size of 1 µm. Most of them were subspherical, and a few irregular particles existed. After hot and cold rolling, the Fe particles underwent plastic deformation and shear fracture, mainly in the shapes of a long strip, fiber, tadpole, spindle, and subspherical. During the rolling process, different shapes of Fe particles were deformed to different degrees.

Table 2
Flow properties of the constituents used in the alloy system [25,26].

Parameters	Cu	Fe
Strain hardening exponent	0.478	0.215
Coefficient of strength (MPa)	459.4	493.3
Tensile strength (MPa)	202	252

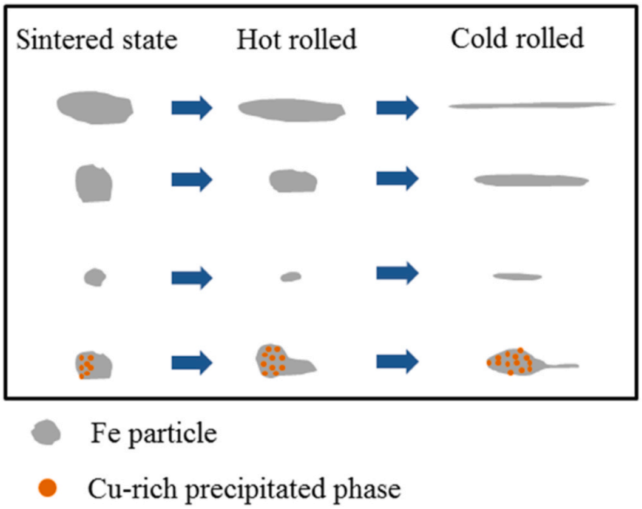

Fig. 12. Schematic diagram related to the deformation of Fe particles in Cu matrix.

The schematic diagram related to the deformation of Fe particles is shown in Fig. 12. The most easily deformed Fe particles were the initial Fe particles in the round bar shape, which had the highest stress along the rolling direction. Next were the tadpole-shaped and ellipsoidal initial Fe particles, which were more difficult to deform overall due to the uneven thickness between the two sides and the center. Finally, the initial near-spherical and spherical Fe particles with smaller sizes were less stressed in the rolling direction, so they were more difficult to deform.

In particular, the Fe particles with the Cu-rich precipitation phase were more difficult to deform than the initial Fe particles. There's a large number of Cu-rich precipitated phases in some Fe particles with spherical shapes and sizes ranging from a few to tens of nanometers in Fig. 8e. It can be seen from the bright-field images that the Cu-rich precipitated phases in Fe particles were distributed at dislocations and grain boundaries. These Cu-rich precipitated phases impeded dislocations slip and grains rotation inside the Fe particles during the deformation process, increasing the strength of the part

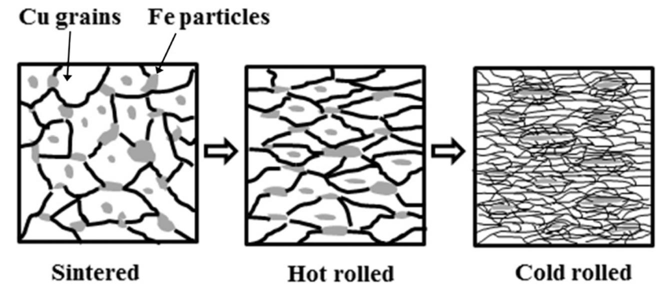

Fig. 13. Schematics of Cu grain refinement mechanisms by Fe particles during deformation.

containing precipitated phases, and weakening their deformation capacity. While some areas without precipitated phases and with smaller thicknesses had low strength and high stress during deformation, some Fe particles underwent local "necking" and formed unique shapes such as "barbell shape". Some round bar-shaped Fe particles with uneven thickness formed long strips under stress and finally "necking" occurred, forming two small independent strips by complete fracture. The development of "necking" also ensured sufficient strain compatibility between the Fe particles and the Cu matrix, thus avoiding residual stress and crack formation.

Compared with Fe, Cu was relatively soft. In the process of deformation, the softer Cu phase was more likely to elongate along the rolling direction, resulting in shear friction. When the shear stress was greater than the tensile strength of Fe, the Fe particles "necked out" and finally fractured when the stress was large enough. The adjacent Cu phase filled the neck and fractured areas. As seen in Fig. 8, the Cu grains around the Fe grains were much finer than the other grains in the area, and there were both fine and coarse grain areas, which indicated that there was severe shear friction deformation between the Fe grains and the surrounding Cu grains during rolling, so that the Cu grains were broken and refined. At the same time, the heat of deformation at the phase interface caused dynamic recrystallization and grain refinement in some regions. As the size of Cu grains near the Fe phase decreased, the strength of the fine-grained region increased compared to other regions. During the cold rolling process, the fine crystal layer of Cu grains around the Fe particles extended to other regions. As the strain increased, the complicated behavior including dislocations propagation, cross-slip migration, and dislocation cells generation and polygonization occurred after the elongation, fragmentation, and refinement of Cu grains, transforming from large grains at the beginning to ultrafine nano-grains [40]. Fig. 13 shows the schematic refinement mechanisms of Fe relative to Cu grains during rolling. In addition, due to the presence of Cu grains, the stress concentration at the interface of Fe particles was reduced, which inhibited the nucleation of deformation twins in Cu grains and avoided the induction of cracks at grain boundaries by deformation twins [39].

5.2. Strengthening mechanisms

The optimum comprehensive performance of Cu-30Fe alloys was obtained after cold rolling and annealing at 400 °C for 1 h. In summary, the strengthening mechanisms were mainly precipitation strengthening, grain boundary strengthening, and strain strengthening. To reveal the strengthening mechanism of the alloy, the strength of the above alloys was calculated by using strengthening models in this paper. The Orowan mechanism is an important strengthening mechanism for aging strengthened Cu alloys, where dislocations interacted with precipitated Fe nanoparticles in the Cu alloy matrix to strengthen the Cu matrix. The strengthening mechanism that bypasses the non-deformable particles can be expressed by the Orowan-Ashby equation [41]:

Table 3
Parameters used in the yield strength model.

Parameter	Value	Units	Ref.
M	3.08	–	[29]
G	46	GPa	[29]
b	0.2556	nm	[29]
υ	0.34	–	[29]
d_p	25	nm	This work
$f\upsilon$	3.5	%	This work
$\triangle\sigma_{Orowan}$	89	MPa	This work
k	0.14	MPa·m	[30]
d_{grain}	0.54	µm	This work
$\triangle\sigma_{GB}$	257	MPa	This work
σ_C	265	MPa	This work
α	0.26	–	[33]
ρ	1.7 × 100	μm^{-2}	This work
$\triangle\sigma_{Work}$	108	MPa	This work

$$\triangle\sigma_{Orowan} = 0.81\frac{MGb}{2\pi(1-\upsilon)^{\frac{1}{2}}}\ \frac{In\left(\frac{d_p}{b}\right)}{\frac{1}{2}d_p\sqrt{\frac{3\pi}{2f_\upsilon}}-d_p} \tag{11}$$

Here, M is the Taylor factor, G is the shear modulus of the Cu matrix, b is the Burgers vector, υ is the Poisson's ratio, d_p is the average size of the precipitated phase (measured by image processing software based on the TEM micrographs in this work), and f_υ is the volume fraction of the precipitated phase. The Fe phase was selected for calculation in this work, and the total volume fraction of the Fe phase was 3.5% and the average diameter was 25 nm. The parameters and calculated results of the Orowan strengthening are listed in Table 3, and the yield strength increased by 89 MPa.

The effect of grain boundaries on yield stress can be calculated using the Hall-Petch equation [42]:

$$\triangle\sigma_{GB} = \mathrm{k}\,d^{-\frac{1}{2}} \tag{12}$$

Here, k is the constant for Cu alloy, and d is the average grain diameter of the Cu matrix (the average grain size was obtained from the EBSD results). In this study, the grain boundary strengthening effect of Cu-Fe alloys can be calculated using the rule of mixtures [43,44]:

$$\sigma_C = \sigma_{Cu}f_{Cu} + \sigma_{Fe}f_{Fe} \tag{13}$$

Here, f_{Cu} is the fraction of the Cu phase, and f_{Fe} is the fraction of the Fe phase. The calculated grain boundary strengthening contribution is 265 MPa.

After the cold rolling process, the dislocation density in the alloy increases significantly, leading to work hardening. The enhancement in yield stress caused by the increase in dislocation density can be calculated by using the Taylor's Eq. (14) [45,46]:

$$\triangle\sigma_{Work} = M\alpha Gb\sqrt{\rho} \tag{14}$$

$$\rho = \sqrt{\frac{16.1\times\varepsilon^2}{b^2}} \tag{15}$$

Here, M is the Taylor factor, α is a geometric constant, G is the shear modulus, b is the Burgers vector of Cu, ρ is the dislocation density (calculated by the Williamson-Hall method using Eq. 15 [47]), and ε is the microstrain calculated from X-ray diffraction results. The calculated value of the work hardening is 108 MPa.

Due to the very small solid solution of Fe in the Cu matrix [48], the present work neglects the increase in the strength of the solid solution by Fe. Finally, the total yield strength of the Cu-Fe alloy can be calculated as:

$$\sigma_{total} = \sigma_0 + \triangle\sigma_{Orowan} + \triangle\sigma_{GB} + \triangle\sigma_{Work} \tag{16}$$

Here, σ_0 is the intrinsic lattice strength, which is estimated to be

60 MPa [42]. The calculated σ_{total} is 522 MPa, which is close to the experimental value of 535 MPa.

6. Conclusions

(1) The thermodynamic calculations showed that the Cu-30Fe alloy with high positive mixing enthalpy formed supersaturated solid solution rather than the amorphous phase by mechanical alloying.

(2) Powder metallurgy Cu-30Fe alloy with fine and uniform Fe particles was prepared. After annealing at 400 °C for 1 h and cold rolling, the Cu-30Fe alloy had a tensile strength of 621 MPa, an elongation of 10.1%, and electrical conductivity of 50.2% IACS, achieving a good combination of mechanical and functional properties.

(3) The Cu matrix surrounded the Fe phase, and the Fe phase would be deformed synergistically with the Cu matrix as a hard phase. Fe particles were elongated into special shapes such as long strips, tadpoles, and spindle shapes during the rolling process.

(4) The refinement of Cu grains was affected by Fe particles during the deformation process. The fine layer of crystalline Cu grains around the Fe particles extended to other regions, thus refining the Cu grains.

(5) The strengthening mechanisms of the Cu-30Fe alloy were the Orowan strengthening, grain boundary strengthening, and strain strengthening, which incresed the yield strength by 89 MPa, 265 MPa, and 108 MPa, respectively. The main strengthening mechanism of the alloy was grain boundary strengthening.

CRediT authorship contribution statement

Chenzeng Zhang: Methodology, Validation, Investigation, Resources, Writing – original draft, Visualization. **Cunguang Chen**: Conceptualization, Methodology, Validation, Writing – review & editing, Supervision, Funding acquisition. **Li Pei**: Resources, Formal analysis, Data curation. **Mengjie Yan**: Resources, Formal analysis, Data curation. **Qian Qin**: Resources, Formal analysis, Data curation. **Fang Yang**: Resources, Formal analysis. **WenWen Wang**: Resources, Formal analysis. **Zhimeng Guo**: Methodology, Resources, Funding acquisition. **Alex A. Volinsky**: Data processing and paper corrections.

Data Availability

The raw/processed data required to reproduce these findings cannot be shared at this time as the data also forms part of an ongoing study.

Declaration of Competing Interest

The authors declare that they have no known competing financial interests or personal relationships that could have appeared to influence the work reported in this paper.

Acknowledgments

This work was supported by the National Natural Science Foundation of China (92066205, U21A200305), the National Natural Science Foundation for Distinguished Young Scholars of China (51925401), and the Fundamental Research Funds, China for the Central Universities (FRF-MP-20-52). AAV acknowledges support by the Mega grant from the Government of the Russian Federation No. 220 of 9 April 2010 (Agreement No. 075-15-2021-612 of 4 June 2021).

References

[1] T. Yamashita, N. Koga, T. Kawasaki, S. Morooka, S. Tomono, O. Umezawa, S. Harjo, Work hardening behavior of dual phase copper–iron alloy at low temperature, Mater. Sci. Eng. A 819 (2021) 141509, https://doi.org/10.1016/j.msea.2021.141509

[2] N. Koga, W. Zhang, S. Tomono, O. Umezawa, Microstructure and low temperature tensile properties in Cu-50 mass%Fe Alloy, Mater. Trans. 62 (2021) 57–61, https://doi.org/10.2320/matertrans.MT-M2020260

[3] Z.W. Wu, Y. Chen, L. Meng, Z. Zhang, Effect of Fe content on the microstructure and mechanical and electrical properties of Cu-Fe in situ composites, J. Mater. Eng. Perform. 30 (2021) 5939–5946, https://doi.org/10.1007/s11665-021-05579-6

[4] J.T. Zhang, W.X. Hao, J.B. Lin, Y.H. Wang, H.Q. Chen, Effects of carbon element on the formed microstructure in undercooled Cu–Fe–C alloys, J. Alloy. Compd. 827 (2020) 154285, https://doi.org/10.1016/j.jallcom.2020.154285

[5] Y. Nakagawa, Liquid immiscibility in copper-iron and copper-cobalt systems in the supercooled state, Acta Mater. 6 (1958) 704–711, https://doi.org/10.1016/0001-6160(58)90061-0

[6] W.L. Wang, Y.H. Wu, L.H. Li, W. Zhai, X.M. Zhang, B. Wei, Liquid-liquid phase separation of freely falling undercooled ternary Fe-Cu-Sn alloy, Sci. Rep. 5 (2015) 16335–16344, https://doi.org/10.1038/srep16335

[7] Y.B. Jeong, H.R. Jo, J.T. Kim, S.H. Hong, K.B. Kim, A study on the micro-evolution of mechanical property and microstructures in (Cu-30Fe)-2X alloys with the addition of minor alloying elements, J. Alloy. Compd. 786 (2019) 341–345, https://doi.org/10.1016/j.jallcom.2019.01.169

[8] H.R. Jo, J.T. Kim, S.H. Hong, Y.S. Kim, H.J. Park, W.J. Park, J.M. Park, K.B. Kim, Effect of silicon on microstructure and mechanical properties of Cu-Fe alloys, J. Alloy. Compd. 707 (2017) 184–188, https://doi.org/10.1016/j.jallcom.2016.12.352

[9] Y.B. Jeong, H.R. Jo, H.J. Park, H. Kato, K.B. Kim, Mechanical properties and microstructural change in (Cu–Fe) immiscible metal matrix composite: effect of Mg on secondary phase, J. Mater. Res. Technol. 9 (2020) 15989–15995, https://doi.org/10.1016/j.jmrt.2020.11.049

[10] D. Yuan, H. Zeng, X.P. Xiao, H. Wang, B.J. Han, B.X. Liu, B. Yang, Effect of Mg addition on Fe phase morphology, distribution and aging kinetics of Cu-6.5Fe alloy, Mater. Sci. Eng. A 812 (2021) 141064, https://doi.org/10.1016/j.msea.2021.141064

[11] S.C. Liu, S.S. Xu, J.C. Jie, J.J. Zhang, Y. Dong, X.Z. Li, T.J. Li, Microstructure evolution and magnetic properties of metastable immiscible Cu-Fe alloy with micro-alloying B element, J. Alloy. Compd. 888 (2021) 161627, https://doi.org/10.1016/j.jallcom.2021.161627

[12] Y.J. Pang, G.H. Chao, T.Y. Luan, S. Gong, Y.R. Wang, Z.H. Jiang, X. Zhu, Y.B. Jiang, Z. Li, Microstructure and properties of high strength, high conductivity and magnetic Cu–10Fe-0.4Si alloy, Mater. Sci. Eng. A 826 (2021) 142012, https://doi.org/10.1016/j.msea.2021.142012

[13] P. Zhang, Q. Lei, X.B. Yuan, X.F. Sheng, D. Jiang, Y.P. Li, Z. Li, Microstructure and mechanical properties of a Cu-Fe-Nb alloy with a high product of the strength times the elongation, Mater. Today Commun. 25 (2020) 101353, https://doi.org/10.1016/j.mtcomm.2020.101353

[14] M. Wang, R. Zhang, Z. Xiao, S. Gong, Y.B. Jiang, Z. Li, Microstructure and properties of Cu-10 wt%Fe alloy produced by double melt mixed casting and multi-stage thermomechanical treatment, J. Alloy. Compd. 820 (2020), https://doi.org/10.1016/j.jallcom.2019.153323

[15] M. Wang, Y.B. Jiang, Z. Li, Z. Xiao, S. Gong, W.T. Qiu, Q. Lei, Microstructure evolution and deformation behaviour of Cu-10 wt%Fe alloy during cold rolling, Mater. Sci. Eng. A 801 (2021) 140379, https://doi.org/10.1016/j.msea.2020.140379

[16] B.X. Song, T.B. Yu, X.Y. Jiang, W.C. Xi, X.L. Lin, Effect of W content on the microstructure and properties of Cu-Fe alloy, J. Mater. Res. Technol. 9 (2020) 6464–6474, https://doi.org/10.1016/j.jmrt.2020.04.031

[17] X.Q. Dai, M. Xie, S.F. Zhou, C.X. Wang, M.H. Gu, J.X. Yang, Z.Y. Li, Formation mechanism and improved properties of Cu95Fe5 homogeneous immiscible composite coating by the combination of mechanical alloying and laser cladding, J. Alloy. Compd. 740 (2018) 194–202, https://doi.org/10.1016/j.jallcom.2018.01.007

[18] X.Q. Dai, S.F. Zhou, M.F. Wang, J.B. Lei, M. Xie, H.N. Chen, C.X. Wang, T. Wang, Effect of substrate types on the microstructure and properties of Cu65Fe35 composite coatings by laser induction hybrid cladding, J. Alloy. Compd. 722 (2017) 173–182, https://doi.org/10.1016/j.jallcom.2017.06.064

[19] A. Chatterjee, E. Sprague, J. Mazumder, A. Misra, Hierarchical microstructures and deformation behavior of laser direct-metal-deposited Cu–Fe alloys, Mater. Sci. Eng. A 802 (2021) 140659, https://doi.org/10.1016/j.msea.2020.140659

[20] Y.D. Li, X.B. Yuan, B.B. Yang, X.J. Ye, P. Zhang, H.Y. Lang, Q. Lei, J.T. Liu, Y.P. Li, Hierarchical microstructure and strengthening mechanism of Cu-36.8Fe alloy manufactured by selective laser melting, J. Alloy. Compd. 895 (2021) 162701, https://doi.org/10.1016/j.jallcom.2021.162701

[21] M. Xie, S.F. Zhou, S.Z. Zhao, D. Chen, L.C. Zhang, In-situ Fe_2P reinforced bulk Cu-Fe immiscible alloy with nanotwinned Cu produced by selective laser melting, J. Alloy. Compd. 838 (2020) 1–6, https://doi.org/10.1016/j.jallcom.2020.155592

[22] N. Koga, S. Tomono, O. Umezawa, Low-temperature tensile properties of Cu-Fe laminated sheets with various number of layers, Mater. Sci. Eng. A 811 (2021) 141066, https://doi.org/10.1016/j.msea.2021.141066

[23] J.M. Guo, Q.Q. Shao, O. Renk, L. Li, Y.B. He, Z.L. Zhang, R. Pippan, Combined Fe and O effects on microstructural evolution and strengthening in Cu–Fe nanocrystalline alloys, Mater. Sci. Eng. A 772 (2020) 138800, https://doi.org/10.1016/j.msea.2019.138800

[24] S.F. Abbas, K.T. Park, T.S. Kim, Effect of composition and powder size on magnetic properties of rapidly solidified copper-iron alloys, J. Alloy. Compd. 741 (2018) 1188–1195, https://doi.org/10.1016/j.jallcom.2018.01.245

[25] S.F. Abbas, T.S. Kim, Effect of lattice strain on the electrical conductivity of rapidly solidified copper-iron metastable alloys, J. Alloy. Compd. 732 (2018) 129–135, https://doi.org/10.1016/j.jallcom.2017.10.180

[26] F.L. Wang, K. Wakoh, Y.P. Li, S. Ito, K. Yamanaka, Y. Koizumi, A. Chiba, Study of microstructure evolution and properties of Cu-Fe microcomposites produced by a pre-alloyed powder method, Mater. Des. 126 (2017) 64–72, https://doi.org/10.1016/j.matdes.2017.04.017

[27] A.R. Miedema, Cohesion in alloys fundamentals of a semi-empirical model, Phys. B 100 (1980) 1–28, https://doi.org/10.1016/0378-4363(80)90054-6

[28] A.K. Niessen, A.R. Miedema, Enthalpies of formation of liquid and solid binary alloys based on 3d metals IV, Alloy. Cobalt Phys. B 151 (3) (1988) 401–432, https://doi.org/10.1016/0378-4363(88)90296-3

[29] K. Anton, A.R. Miedema, The Enthalpy effect on forming diluted solid solutions of two 4d and 5d transition metals, Bunsenges. Phys. Chem. 87 (9) (1983) 717–725, https://doi.org/10.1002/bbpc.19830870903

[30] C. Suryanarayana, Mechanical alloying and milling, Prog. Mater. Sci. 46 (2001) 1–184, https://doi.org/10.1016/S0079-6425(99)00010-9

[31] A. Contini, F. Delogu, S. Garroni, G. Mulas, S. Enzo, Kinetics behaviour of metastable equiatomic Cu–Fe solid solution as function of the number of collisions induced by mechanical alloying, J. Alloy. Compd. 615 (2014) S551–S554, https://doi.org/10.1016/j.jallcom.2013.11.232

[32] X. Sauvage, F. Wetscher, P. Pareige, Mechanical alloying of Cu and Fe induced by severe plastic deformation of a Cu–Fe composite, Acta Mater. 53 (7) (2005) 2127–2135, https://doi.org/10.1016/j.actamat.2005.01.024

[33] J.Z. Jiang, R. Bormann, Mechanical alloying in the Fe–Cu system, Mater. Sci. Eng. A 242 (1998) 268–277, https://doi.org/10.1016/S0921-5093(97)00522-4

[34] B. Majumdar, A. Narayanasamyb, K. Chattopadhyay, Structural and magnetic investigations on the metastable phases of the mechanically alloyed Fe-Cu system, J. Alloy. Compd. 248 (1997) 192–200, https://doi.org/10.1016/S0925-8388(96)02422-X

[35] M. Rajagopalan, S. Turnage, R.K. Koju, B. Hornbuckle, Y. Mishin, K.N. Solanki, Microstructural evolution in a nanocrystalline Cu-Ta alloy a combined in-situ TEM and atomistic study, Mater. Des. 113 (2017) 178–185, https://doi.org/10.1016/j.matdes.2016.10.020

[36] S.L. Semiatin, H.R. Piehler, Formability of sandwich sheet materials in plane strain compression and rolling, Metall. Mater. Trans. A 10 (1979) 97–107, https://doi.org/10.1007/BF02686412

[37] Y.M. Hwang, H.H. Hsu, H.J. Lee, Analysis of plastic instability during sandwich sheet rolling, Int. J. Mach. Tool. Man. 36 (1) (1996) 47–62, https://doi.org/10.1016/0890-6955(95)92628-C

[38] J.M. Lee, B.R. Lee, S.B. Kang, Control of layer continuity in metallic multilayers produced by deformation synthesis method, Mater. Sci. Eng. A 406 (1–2) (2005) 95–101, https://doi.org/10.1016/j.msea.2005.06.030

[39] A. Gilbert, G.T. Hahn, C.N. Reid, B.A. Wilcox, Twin-induced grain boundary cracking in b.c.c, Acta Mater. 12 (1964) 754–755, https://doi.org/10.1016/0001-6160(64)90230-5

[40] Y.P. Li, Z. Xiao, Z. Li, Z.Y. Zhou, Z.Q. Yang, Q. Lei, Microstructure and properties of a novel Cu-Mg-Ca alloy with high strength and high electrical conductivity, J. Alloy. Compd. 723 (2017) 1162–1170, https://doi.org/10.1016/j.jallcom.2017.06.155

[41] L. Wu, Renormalized energy for dislocations in quasi-crystals, Nonlinear Anal. 156 (2017) 167–196, https://doi.org/10.1016/j.na.2017.02.018 real..

[42] M. Furukawa, Z. Horita, M. Nemoto, R. Valiev, T.G. Langdon, Structural evolution and validity of Hall-Petch relationship in an Al-3% Mg alloy with submicron grain size, Mater. Sci. Forum 204–206 (1996) 431–436, https://doi.org/10.4028/www.scientific.net/MSF.204-206.431

[43] W.A. Spitzig, A.R. Pelton, F.C. Laabs, Characterization of the strength and microstructure of heavily cold worked Cu-Nb composites, Acta Mater. 35 (10) (1987) 2427–2442, https://doi.org/10.1016/0001-6160(87)90140-4

[44] B.D. Sun, H.Y. Gao, J. Wang, D. Shu, Strength of deformation processed Cu–Fe–Ag in situ composites, Mater. Lett. 61 (4–5) (2007) 1002–1006, https://doi.org/10.1016/j.matlet.2006.06.030

[45] Y. Wu, Y. Li, J.Y. Lu, S. Tan, F. Jiang, J. Sun, Correlations between microstructures and properties of Cu-Ni-Si-Cr alloy, Mater. Sci. Eng. A 731 (2018) 403–412, https://doi.org/10.1016/j.msea.2018.06.075

[46] R.G. Li, S.R. Zhang, C.L. Zou, H.J. Kang, T.M. Wang, The roles of Hf element in optimizing strength, ductility and electrical conductivity of copper alloys, Mater. Sci. Eng. A 758 (2019) 130–138, https://doi.org/10.1016/j.msea.2019.04.110

[47] R.P. Shi, C.P. Wang, D. Wheeler, X.J. Liu, Y. Wang, Formation mechanisms of self-organized core/shell and core/shell/corona microstructures in liquid droplets of immiscible alloys, Acta Mater. 61 (4) (2013) 1229–1243, https://doi.org/10.1016/j.actamat.2012.10.033

[48] D. Li, M.B. Robinson, T.J. Rathz, G. Williams, Liquidus temperatures and solidification behavior in the copper–niobium system, Acta Mater. 46 (11) (1998) 3849–3855, https://doi.org/10.1016/S1359-6454(98)00063-9